Article

Imaging Reaction Dynamics of F⁻(H₂O) and Cl⁻(H₂O) with CH₃I

Björn Bastian, Tim Michaelsen, Lulu Li, Milan Ončák, Jennifer Meyer, Dong H. Zhang, and Roland Wester*

Cite This: *J. Phys. Chem. A* 2020, 124, 1929–1939

Read Online

ACCESS | Metrics & More | Article Recommendations | Supporting Information

ABSTRACT: The dynamics of microhydrated nucleophilic substitution reactions have been studied using crossed beam velocity map imaging experiments and quasiclassical trajectory simulations at different collision energies between 0.3 and 2.6 eV. For $F^-(H_2O)$ reacting with CH_3I, a small fraction of hydrated product ions $I^-(H_2O)$ is observed at low collision energies. This product, as well as the dominant I^-, is formed predominantly through indirect reaction mechanisms. In contrast, a much smaller indirect fraction is determined for the unsolvated reaction. At the largest studied collision energies, the solvated reaction is found to also occur via a direct rebound mechanism. The measured product angular distributions exhibit an overall good agreement with the simulated angular distributions. Besides nucleophilic substitution, also ligand exchange reactions forming $F^-(CH_3I)$ and, at high collision energies, proton transfer reactions are detected. The differential scattering images reveal that the $Cl^-(H_2O) + CH_3I$ reaction also proceeds predominantly via indirect reaction mechanisms.
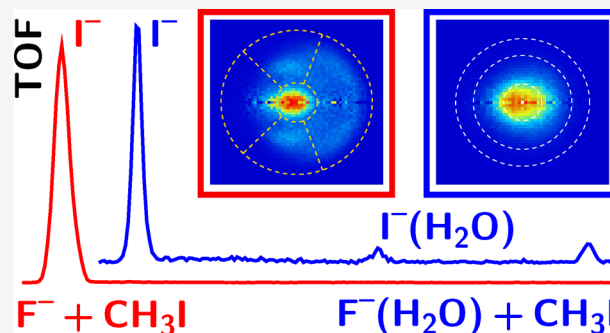
1. INTRODUCTION

Reaction dynamics of the important class of bimolecular nucleophilic substitution (S_N2) reactions have been studied extensively for $X^- + CH_3Y$ model systems with several combinations of halide anions and methyl halides.[1−5] Detailed information on gas phase reaction dynamics is obtained by measuring differential cross sections of bimolecular reactions in crossed molecular beams under single collision conditions. The in-depth gas phase picture obtained from experimental evidence and simulations often provides a good starting point to interpret reaction dynamics in liquids, which has become experimentally accessible by time-resolved infrared spectroscopy.[6]

The gas phase approach to understanding solvent effects in ion−molecule reactions is the addition of single solvent molecules to the nucleophile, which is referred to as microsolvation.[7] Especially in the case of protic solvents, preferential stabilization of the reactants relative to the transition state leads to transition from a double-well potential energy surface (PES) in the gas phase to a higher reaction barrier and unimodal profile in solution.[8] The consequence is smaller reaction rates by several orders of magnitude. If the solvent cannot rearrange to follow charge in the reaction intermediate, desolvation of the reactants and unsolvated products imply a lower exothermicity. Therefore, already the addition of a few solvent molecules will strongly quench the reaction.[9,10] This effect is important in microsolvated S_N2 reactions that typically avoid the energetically favored solvated products—as opposed to reactions in solution where different

molecules concertedly desolvate the nucleophile and solvate the leaving group.[11] When S_N2 reactions become inefficient by stepwise solvation, ligand exchange can become important as has been reported for $Cl^-(D_2O)_{1-3}$ and $F^-(H_2O)_{4-5}$ reactions with CH_3Br.[12,13]

This work focuses on the highly exothermic halide-exchange S_N2 reaction $F^-(H_2O) + CH_3I$ with a single water solvent. The reactivity of the $F^- + CH_3I$ reaction at 302(2) K decreases from $19.4(2) \times 10^{-10}$ cm³ s⁻¹ for the solvent-free case to $8.64(9) \times 10^{-10}$ cm³ s⁻¹ upon single H_2O solvation of the anion, whereas reactivity is decreased by a factor of 100 in the less exothermic reaction with CH_3Cl. The observed I^- to $I^-(H_2O)$ product branching is 9:1.[14]

The PESs of the reactions with $F^-(H_2O)$[15] and $OH^-(H_2O)$[16] are overall similar to those of the water-free systems. They allow initial association either in a hydrogen-bonded $X^-(H_2O)\cdots HCH_2I$ complex or in an ion−dipole $X^-(H_2O)\cdots CH_3I$ complex with a small barrier in between. According to the energetics, the latter may undergo Walden inversion with the water molecule, driven by H-bonding to the halide atoms, shifting to the iodine side. However, atomistic dynamics deviate considerably from the intrinsic reaction coordinate, as more than 90% of the reactive trajectories avoid

water-bound postreaction complexes in low energy collisions.[17] Single water molecules mostly dissociate from F^- at the moment of nucleophilic displacement. In the case of higher hydrated F^- ions, additional water molecules detach early in the entrance channel and S_N2 occurs through the less solvated barrier with higher energy but diminished steric hindrance.[18] Direct dynamics studies on the related reactions of $F^-(H_2O)$ and $OH^-(H_2O)$ with CH_3Cl have revealed a strong effect of the relative H_2O position in the entrance geometry on product channels and reaction probability.[19,20]

Computed reactive cross sections for $F^-(H_2O)$ + CH_3I collisions at 0.32 eV yield 4.4(13)% $I^-(H_2O)$, 9(6)% $CH_3F(H_2O)$, and three-body dissociation in most cases.[17] For all three channels, indirect mechanisms are dominant with fractions of about 70%, of which ca. 90% pass through the hydrogen-bonded prereaction complex. Also direct rebound (DR) is reported for all three channels, whereas direct stripping (DS) always leads to I^- formation. High level ab initio stationary points suggest additional mechanisms at higher collision energies such as front-side attack, double inversion, and proton transfer from H_2O to F^- followed by OH^- driven S_N2 forming methanol.[21] Proton transfer from CH_3I opens at much higher collision energies.[22]

At 1.53 eV collision energy, direct dynamics simulations do not observe any $I^-(H_2O)$ and only 1.2(5)% $CH_3F(H_2O)$.[23] In about 70% of the indirect reactions, water dissociates at the initial collision. Subsequently, the water-free prereaction complexes are formed such that S_N2 resembles ligand exchange followed by fragmentation of the FCH_3I^- complex. Indirect mechanisms still dominate at higher energy, which is attributed to steric effects. The early dehydration favors nucleophilic attack and therefore attenuates the suppression of reactivity by the solvent. Furthermore, methanol formation is indeed observed in about 10% of the trajectories.

When the nucleophile is changed to $Cl^-(H_2O)$, only an ion—dipole complex is found in the entrance channel.[24] The predominant mechanism at high collision energies is direct rebound instead of indirect mechanisms, and a roundabout mechanism dominates indirect reactions instead of complex formation. At 1.9 eV, simulations found early water loss, which leads to similar reaction probabilities, mechanisms, and energy and angular distributions as in the unsolvated reaction.[24] At lower collision energies, different solvated dynamics are expected, as also the Cl^- + CH_3I mechanisms depend significantly on collision energy.

Previous crossed beam experiments and direct dynamics simulations on the solvent-free F^- + CH_3I reaction revealed the importance of a hydrogen-bonded prereaction complex that leads to deviations from the traditional Walden inversion pathway.[25] Also a halogen-bonded front-side complex is important at low collision energies.[26,27] Complex formation results in a large contribution of indirect dynamics to the scattering images which was unexpected and is still important at rising collision energies.[28] Agreement of energy and angular distributions with simulation results also permitted identification of direct stripping as a third mechanism. Furthermore, two retention pathways have been found as minor pathways based on trajectories on an accurate analytical PES[29] and competing reaction channels at higher collision energies have also been experimentally investigated.[30] In the Cl^- + CH_3I system, complex formation does not occur and dominant indirect dynamics is only observed at low collision energies. Scattering images at 1.1 eV reveal direct rebound as the

predominant mechanism,[31] indicative for a collinear approach with Walden inversion. An indirect roundabout mechanism appears at 1.9 eV and has been characterized using direct dynamics simulations.[32]

Simulations of reaction dynamics under microsolvation have been extended to non-halide anions[33] and reactions with ethyl halides[34] that involve intricate competition effects with the additional E2 elimination channel.[35,36] At the same time, extensive experimental results on reaction dynamics of these systems have only been reported for the $OH^-(H_2O)_n$ + CH_3I reaction. Previous crossed beam studies with our setup cover different solvation levels n = 0, 1, 2 in the 0.5−2 eV collision energy range[37,38] and variation of the anion water cluster temperature.[39] Most interestingly, the hydrogen-bonded complex, similar to the isoelectronic reaction with F^-, avoids the traditional collinear nucleophilic attack—but addition of a single water molecule sterically facilitates the collinear approach and therefore enhances direct rebound at intermediate and high collision energies.[37] Upon addition of a second water molecule, direct mechanisms are completely suppressed.

In order to test the different theoretical simulations, insight from reactive scattering experiments is needed. In the present work, the differential scattering cross sections have been studied for the reactions of $F^-(H_2O)$ and $Cl^-(H_2O)$ with CH_3I using crossed beam ion imaging. This allows for detailed information on the atomistic dynamics and the interplay of different reaction mechanisms. In particular, it provides a test of the product branching ratios and sheds new light on the effect of the solvent molecule on the atomistic reaction dynamics. Improved data for the unsolvated reaction F^- + CH_3I allows us to extract the relative contributions of different atomistic mechanisms in the S_N2 reaction. Furthermore, the $Cl^-(H_2O)$ data provide insight into the role of the nucleophile and complement recent direct dynamics simulations with experimental evidence at lower collision energies.

2. EXPERIMENTAL AND THEORETICAL METHODS

2.1. Crossed Beam Imaging. Angle and energy differential cross sections of the charged products of ion—molecule reactions are measured by three-dimensional velocity map imaging[40] (VMI) in a crossed beam setup.[41] Precursor gases are ionized by plasma discharge in a supersonic expansion from a pulsed piezo cantilever valve. Ions are then thermalized in a radio frequency trap[37] with room temperature buffer gas, in the present work typically argon. After 40 ms, ions are accelerated to the desired kinetic energy and cross a molecular beam that is seeded with the neutral reactant in the center of the VMI spectrometer. Position and flight time are recorded by a combination of multichannel plates with a phosphor screen, digital camera, and photomultiplier tube. Product ions are discriminated by their flight time, and each pair of position and time is converted into the velocity vector in the center-of-mass frame. Symmetry about the collision axis permits mapping of the velocity vectors to two components parallel (v_x) and perpendicular (v_r) to the axis. To mimic slice distributions in the scattering plane, ion counts are weighted by v_r^{-1}. Background from the ion beam is recorded with asynchronous timing of the neutral beam and subtracted. Collision energy and center-of-mass velocity in the scattering plane are determined from ion and neutral beam distributions recorded by two-dimensional VMI. For this, the neutral beam is ionized by electron impact.

For comparison with measured arrival times on the VMI detector, flight times of ions with different masses were determined from ion trajectory simulations using SIMION.[42] In particular, simulations have been performed for metastable product ion complexes that may dissociate during acceleration in the field of the VMI spectrometer. Apparent masses as a function of the moment of dissociation were calculated in steps of 0.2 μs. Details about the specific VMI geometry and potentials have been published in ref 43.

F^- anions were formed from NF_3 diluted in argon. The same mixture was bubbled through distilled water in a gas washing bottle with filter plate in order to have $F^-(H_2O)$ clusters form in the dense part of the supersonic expansion. As other ions (FHO^-, F_2^-, and HF_2^-) with close-lying masses were also present in the plasma, mass separation was required to prepare the $F^-(H_2O)$ reactant. Time-of-flight separation together with pulsed opening of the radio frequency trap allowed for the manipulation of the reactant ion composition and suppression of the unwanted coreactants. The reactant branching ratios were estimated from time-of-flight traces obtained by velocity mapping of the ion beam at the same moment at which product ions were imaged in reactive scattering. Overshoots in the time-of-flight traces were approximately corrected.[44] At 2.6 eV collision energy, two measurements were performed with H_2 instead of Ar buffer gas to further suppress FHO^- contamination. At the same time, the amount of HF_2^- could be reduced by earlier timing of the trap entrance. The remaining amount of coreactants has been found to have only a minor relevance for the results on the $F^-(H_2O)$ reactions (see the Supporting Information).

Cl^- anions were formed from CH_3Cl diluted in argon with a pulsed discharge stabilized by a static electron source. Dissolution of air in the distilled water bottle was found to lead to the formation of the unwanted coreactant $O_2^-(H_2O)$. To avoid this, a pure $Cl^-(H_2O)$ reactant beam was obtained without the washing bottle after pure water was accumulated in the mixing bottle of the precursor gas.

2.2. Electronic Structure Calculations and Dynamical Simulations. Ab initio calculations at the coupled cluster singles and doubles (CCSD) level using the aug-cc-pVTZ-PP basis set for iodine and the aug-cc-pVTZ basis set for all other elements, further denoted as CCSD/aug-cc-pVTZ(-PP), have been performed to obtain a coherent set of exothermicities for the reactive channels of the CH_3I reaction with the anions of interest F^-, $F^-(H_2O)$, and $Cl^-(H_2O)$ using the Gaussian 16 program.[45] Further computations have been performed for the unwanted coreactants FHO^-, F_2^-, and HF_2^-. Wave function stabilization was performed for every structure. Zero-point energy is included in all reported energies. Energetics and structural data for all anions is given in the Supporting Information. Analysis of the experimental data was based on the following exothermicities of the most probable channels for the respective charged product, which were computed at the CCSD(T) level. The energy levels of the reactants and products of the reaction pathways with F^- and $F^-(H_2O)$ are summarized in Figure 1.
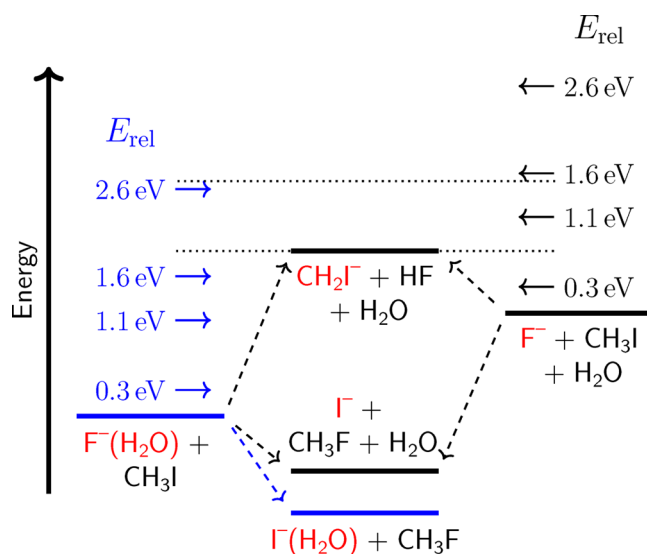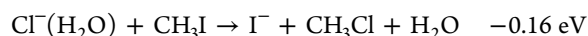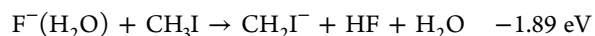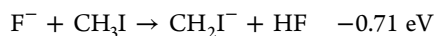
$$F^- + CH_3I \rightarrow I^- + CH_3F \quad 1.81\text{ eV}$$

$$F^-(H_2O) + CH_3I \rightarrow I^- + CH_3F + H_2O \quad 0.63\text{ eV}$$

$$F^-(H_2O) + CH_3I \rightarrow I^-(H_2O) + CH_3F \quad 1.11\text{ eV}$$

$$F^- + CH_3I \rightarrow CH_2I^- + HF \quad -0.71\text{ eV}$$

$$F^-(H_2O) + CH_3I \rightarrow CH_2I^- + HF + H_2O \quad -1.89\text{ eV}$$

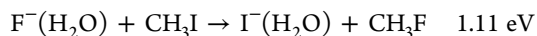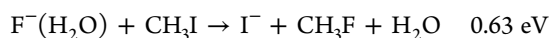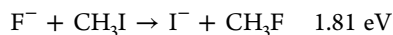$$Cl^-(H_2O) + CH_3I \rightarrow I^- + CH_3Cl + H_2O \quad -0.16\text{ eV}$$

Figure 1. Energy level diagram relating the reactants and products of the monohydrated and solvent-free $F^- + CH_3I$ reactions. Only the S_N2 and proton transfer channels, for which the product velocity images are discussed in the present work, are shown. Different collision energies of the reactive scattering measurements are denoted by arrows above the energy level of the respective reactants. Dotted lines indicate the threshold for the proton transfer channel and collision energies for the two reactions that correspond to similar excess energies above threshold.

For a detailed comparison, we constructed a global PES for the reaction of $F^-(H_2O)$ and CH_3I, using the fundamental invariant neural network (FI-NN[46]) fitting method. With the use of Gaussian 09,[48] 141,921 XYGJ-OS[47]/aug-cc-pVTZ (aug-cc-pVTZ-PP for iodine atom) electronic energies were calculated. XYGJ-OS is a fast doubly hybrid density functional method, whose overall accuracy is close to chemical accuracy.[47] The geometries used in the fitting were properly selected based on direct simulations and further quasiclassical trajectory (QCT) calculations using the preliminary PESs iteratively. The final PES is well-converged with respect to the fitting errors and the results of dynamical simulations. The final fitting root-mean-square error (RMSE) is 13.8 meV for energies up to 3.0 eV relative to the reactant $F^-(H_2O) + CH_3I$.

The QCT simulations were carried out at the collision energies of 0.3, 1.0, and 1.5 eV for the $F^-(H_2O) + CH_3I$ reaction on the new PES described above. Quasiclassical vibrational ground states were prepared for initial reactants $F^-(H_2O)$ and CH_3I by normal mode sampling. The total angular momentum was set to zero by initial momentum adjustments. The initial distance between the centers of mass of $F^-(H_2O)$ and CH_3I was $(x^2 + b^2)^{1/2}$, where b is the impact parameter and x is set to $30a_0$. The orientation of $F^-(H_2O)$ was randomly sampled with respect to CH_3I and b was sampled uniformly between 0 and b_{max}, where the b_{max} values were $18a_0$ at 0.3 eV, $14a_0$ at 1.0 eV, and $12.6a_0$ at 1.5 eV. One million trajectories were computed at each energy. The trajectories were terminated when the distance between the collisional product species (for the channel with three products, the value is defined as the minimum distance

between three species) reached $20a_0$ or the maximum distance among all nine atoms reached $30a_0$.

3. RESULTS

3.1. Product Channels for F⁻(H₂O) Reactions. Product ion mass spectra for the reactions of F^- and $F^-(H_2O)$ with CH_3I at 0.3 eV collision energy in Figure 2 show I^- as the only
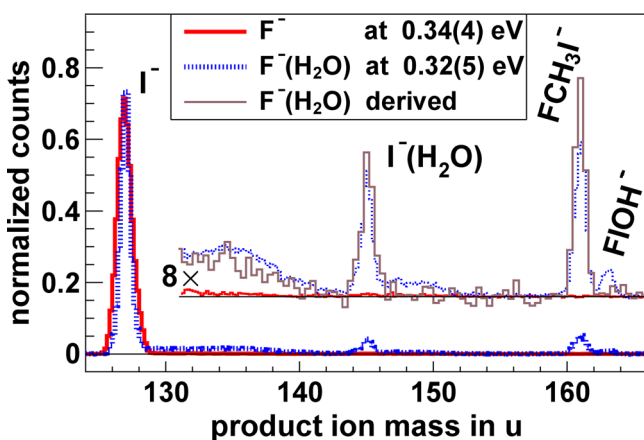

Figure 2. Observed product mass spectra for reactions of CH_3I with F^- and with $F^-(H_2O)$ in the presence of coreactants. A 8× zoom is shown as inset including a mass spectrum for pure $F^-(H_2O)$ derived from three observed spectra with different reactant compositions.

product of the unsolvated reaction. In the singly solvated reaction, the unwanted coreactants FHO^-, F_2^-, and HF_2^- were present at a 3−14% level compared to 100% $F^-(H_2O)$. The contribution of the different reactants to the observed product ions is analyzed in the Supporting Information. Altogether, 6(3)% of the products stem from FHO^-, and the contributions by F_2^- and HF_2^- are bound by upper limits of 1.2(3) and 7(7)%. $F^-(H_2O)$ accounts for at least 86(8) and 94(3)% of the I^- and $I^-(H_2O)$ products. A derived difference mass spectrum for the pure $F^-(H_2O) + CH_3I$ reaction is shown as inset in Figure 2. Besides the main I^- peak, the solvated S_N2 product $I^-(H_2O)$ and the ligand exchange reaction forming FCH_3I^- are observed. In the hydrated reaction, the I^- peak is accompanied by a broad tail of apparently higher masses ranging up to 142 u, which is also assigned to I^- and accounts for 11(3)% of the total I^- signal area. Including the tail contribution, the extracted product branching ratios of the $F^-(H_2O) + CH_3I$ reaction are 89.3(11)% for I^-, 4.5(9)% for $I^-(H_2O)$, and 6.2(7)% for FCH_3I^- at 0.32 eV collision energy. Values in parentheses are statistical errors in units of the last digit. The peak integration procedure involves additional systematic uncertainties at the percent level.

The tail of apparently higher masses up to 142 u can be explained by the dissociation of an intermediate complex, candidates being $I^-(H_2O)$ and FCH_3I^-, in the acceleration region of the VMI spectrometer, which results in a flight time between those of the heavier and lighter species. Further evidence is given by mass spectra at 2.6 eV collision energy with VMI pulses first, as usual, 0.4 µs after the ion beam peak, and second, delayed by another 2.2 µs after the ion packet has passed the VMI center, in order to avoid acceleration of unstable complexes. The late pulse preserves the total I^- intensity and the width of the high mass tail, but reduces the

tail fraction from 38(5) to 25(6)%. We conclude that fewer complexes are accelerated before their final dissociation.

To test this, we have computed apparent masses as a function of dissociation time with respect to the start of VMI acceleration. The result is shown in Figure S3.2. For FCH_3I^- dissociating to I^-, the apparent mass increases by 4 u µs⁻¹ from 127 to 143 u at 4 µs and then, in a region of strong acceleration, by 16 u µs⁻¹ up to 161 u near 5 µs. Mass loss during the onset of strong acceleration in the 3−4 µs range corresponds to apparent masses of 139−144 u. The observed I^- tail vanishes near 142 u, which corresponds to lifetimes near 4 µs.

The fraction of solvated product ions $I^-(H_2O)$ relative to total S_N2 reactivity, derived from the measured product mass spectra, is plotted as a function of collision energy in Figure 3.
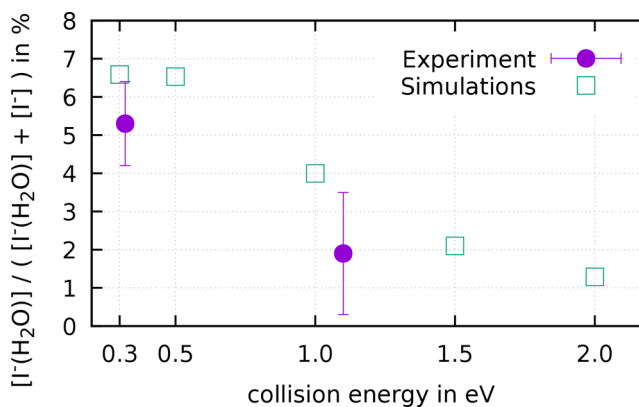

Figure 3. Fraction of $I^-(H_2O)$ from the total S_N2 reactivity in comparison of experiment and theory. Only I^- in the peak at the nominal mass is considered for the experimental value, because products from long-lived intermediates were not traceable in simulations.

All product mass spectra at 1.1, 1.6, and 2.6 eV collision energies, reactant compositions, and integrated product branching ratios are provided in the Supporting Information. With increasing collision energy, the I^- tail to peak fraction rises continuously, roughly doubling from 0.3 eV to the highest energy. At 1 eV, the solvated S_N2 product $I^-(H_2O)$ amounts to about 2%, which is near the detection limit, as is visible from the error bar in Figure 3. In turn, proton transfer opens up at 2 eV and is discussed in section 3.3. Ligand exchange forming FCH_3I^- is slowly suppressed for larger collision energies. Dihalide formation becomes energetically accessible near 2 eV. The formation of FI^- or FHI^- by $F^-(H_2O)$ is compatible with an intensity increase in this mass range at 2.6 eV. An unequivocal assignment to these channels is impeded by the coreactants. However, large differences by factors of 3−6 of the proportion of HF_2^- and FHO^- in the reactant ion beam composition at 2.5 eV collision energy do not have a noticeable effect on the I^- and $I^-(H_2O)$ product ion velocity images, energy, and angular distributions. This justifies interpreting them as results of the $F^-(H_2O) + CH_3I$ reaction not only at 0.3 eV, but also up to the highest investigated collision energy.

Figure 3 also shows the fraction of solvated S_N2 reaction products obtained from the QCT simulations. The trajectory simulations were terminated at a chosen distance between the products. In parts, the obtained FCH_3I^- product complexes may therefore be metastable. For comparison, the experimental

I$^-$(H$_2$O) fractions in Figure 3 were computed without including the I$^-$ tails that stem from late complex dissociation.

3.2. Nucleophilic Substitution of F$^-$ and F$^-$(H$_2$O). The reactions F$^-$ + CH$_3$I and F$^-$(H$_2$O) + CH$_3$I have been measured under similar conditions at four different collision energies ranging from 0.3 to 2.6 eV. Velocity images of the I$^-$ product ion are presented in Figure 4 in the center-of-mass
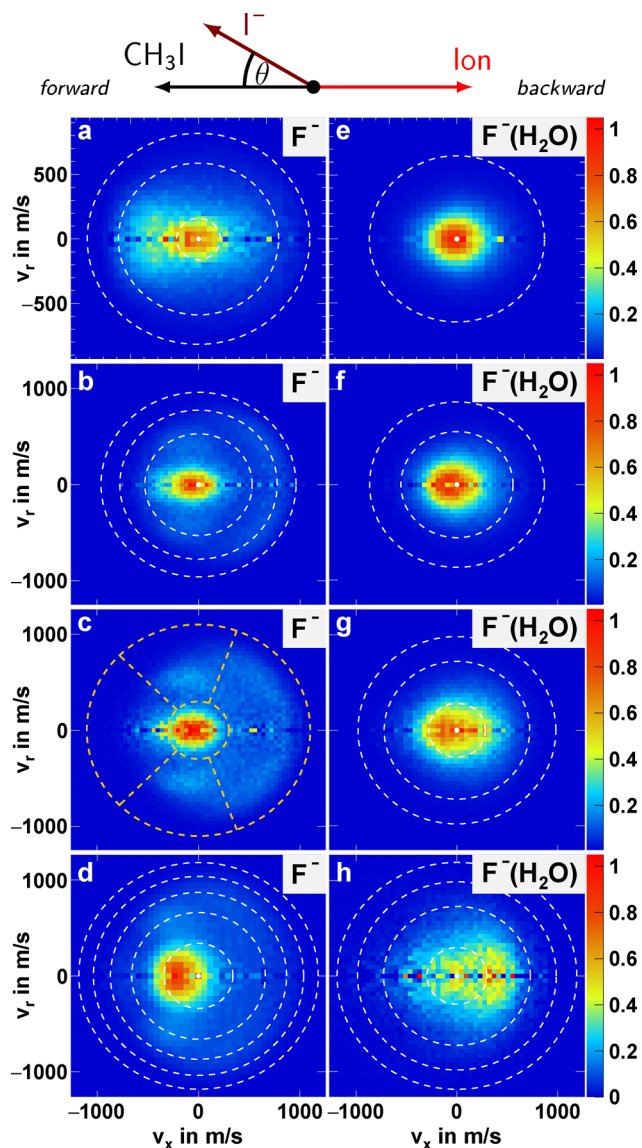

Figure 4. I$^-$ velocity images in center-of-mass frame as depicted by the above Newton diagram. (a−d) F$^-$ + CH$_3$I reaction at 0.27(4), 1.06(8), 1.56(8), and 2.55(10) eV collision energies. (e−h) F$^-$(H$_2$O) + CH$_3$I reaction at 0.32(5), 1.07(7), 1.55(7), and 2.57(11) eV collision energies. Circles indicate the kinematic cutoff and 1 eV steps in terms of higher ΔE that in the case of F$^-$ is identical to E_{int}. (h) Instead of the Newton rings, cuts to different mechanisms are marked in orange.

frame that is depicted by the Newton diagram above. Left and right half-planes correspond to forward and backward scattering of the product ion relative to the neutral reactant. Outer circles indicate the maximum ion kinetic energies (kinematic cutoffs) that correspond to the maximum kinetic energy E'_{rel} of relative motion between the ion and the center of mass of the neutral products. It is given by the sum of the

average collision energy E_{rel} plus the computed exothermicities E_{exo} (see section 2.2). Inner circles correspond to 1 eV differences in terms of lower E'_{rel}. Using the energy difference

$$\Delta E = E_{rel} + E_{exo} - E'_{rel} = E_{int} - E^0_{int} + E^{neutral}_{rel} \quad (1)$$

where $E^{neutral}_{rel}$ denotes the kinetic energy of relative motion between the neutrals, the kinematic cutoff is described by $\Delta E = 0$. $E^{neutral}_{rel}$ is zero in case of a single neutral product such that $\Delta E = E_{int} - E^0_{int}$ gives a direct measure, while in general $\Delta E \geq E_{int} - E^0_{int}$ gives an upper bound to the internal excitation E_{int} of all products. E^0_{int} is dominated by the thermal energy of the anion−water cluster trapped with buffer gas at room temperature. The initial internal excitation energy of reactants E^0_{int} is estimated to be about 0.1 eV under the room temperature conditions of the ion preparation.

The F$^-$ + CH$_3$I → I$^-$ + CH$_3$F reaction has been studied before by our group[28] and is reinvestigated here to allow for a direct comparison with the hydrated reaction. At low energy it exhibits two distinct features in the product ion image (Figure 4a) that indicate different reaction mechanisms. A central and rather isotropic distribution indicates one or several indirect reaction mechanisms with intermediates that live long enough such that initial orientation becomes irrelevant. Energy is redistributed into internal degrees of freedom and peaks at maximum internal excitation. The second pronounced distribution is characterized by forward scattering of the product ion relative to the incoming neutral CH$_3$I which is indicative for a direct mechanism. Product ion images at higher collision energies have been theoretically described by three distinct mechanisms and compared to time-sliced product ion images before.[28]

The improved resolution obtained in the present work now allows us to quantify the fractions of the different mechanisms experimentally. The upper bound fraction of indirect mechanisms is estimated as the isotropic area below the minimum (averaged over a small angular range) of the angular distributions (see Figure S3.1). The remaining area is split into the forward and backward hemisphere and attributed as a lower bound to the direct stripping and direct rebound fractions. In this way, the angular distribution in Figure 5a gives a 12:19:69 ratio for direct rebound, direct stripping, and indirect mechanisms at 0.27 eV. To obtain an improved estimate for the comparison with the computational results, we set an upper limit of 1.2 eV for the internal energy of indirect mechanisms, which yields an isotropic area of 52% relative to total reactivity. At 1.56 eV, the cuts marked with orange lines in Figure 4c are integrated and give 6% forward, 43% sideways, 41% backward, and 10% low energy isotropic scattering. In this case, the 10% gives a lower bound to indirect mechanisms.

For F$^-$(H$_2$O) + CH$_3$I reactions, only indirect mechanisms are evident in the images at collision energies up to 1.6 eV. At 2.6 eV, the visible appearance of a backward scattered distribution in Figure 4h indicates the increasing importance of a direct rebound mechanism at higher energies. This is reflected by the backward tendency of the difference histogram in Figure 5b. The angular distributions at the lower collision energies are very similar to each other. Corresponding scattering angle distributions from QCT simulations are presented in Figure 5c. They show a stronger intensity of small and large scattering angles and a more pronounced shift toward stronger backward scattering already at 1.0 and 1.5 eV collision energies. Except for the outermost bins, the close similarity of angular distributions of I$^-$ and I$^-$(H$_2$O) is
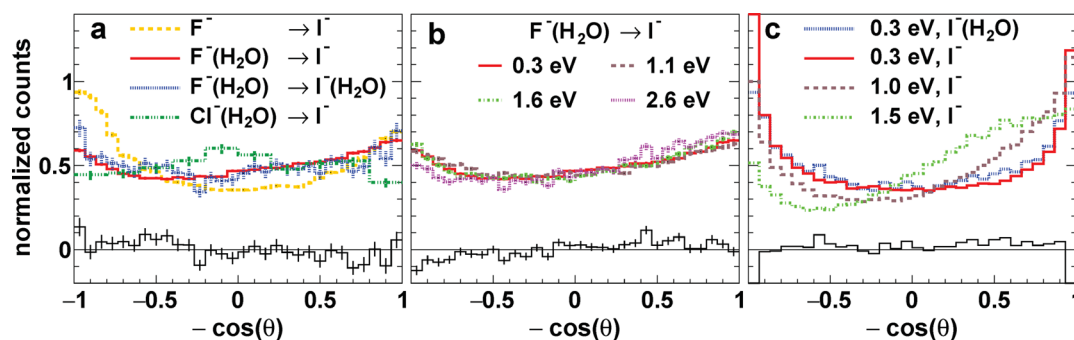
Figure 5. Scattering angle distributions for nucleophilic substitution in reactions with CH_3I. Legends specify reactant and product ions. (a) F^-, $F^-(H_2O)$, and $Cl^-(H_2O)$ at 0.3 eV collision energy. The lower solid black line shows the difference of the $I^-(H_2O)$ and I^- distributions from $F^-(H_2O)$ scattering. (b) $F^-(H_2O)$ at different collision energies. The lower solid black line shows the difference of the 2.6 and 1.6 eV distributions. (c) Distributions for $F^-(H_2O)$ scattering from quasiclassical trajectory simulations. Product ions are specified in the legend. The lower solid black line shows the difference of the $I^-(H_2O)$ and I^- distributions at 0.3 eV.

captured by the QCT simulations (see Figure 5c). The experimental upper bound fraction of indirect mechanisms is again estimated as the isotropic area below the minimum of the angular distributions. Forward and backward contributions are separated near $\cos(\theta) = 0.2$ (see Figure S3.3) and percentages summarized in Table 1.

Table 1. Fractions of Mechanisms in the $F^-(H_2O) \rightarrow I^-$ Channels[a]

	energy (eV)			
	0.3	1.1	1.6	2.6
direct rebound (%)	13 (9)	9	13	19
direct stripping (%)	4 (7)	4	4	2
indirect (%)	83 (84)	87	83	78

[a]Fractions for $I^-(H_2O)$ products are given in parentheses. Uncertainties of about 2% apply to the indirect fractions that are upper bound values.

Images for the solvated S_N2 product $I^-(H_2O)$ and the proton transfer product ion CH_2I^- are shown in Figure 6. At the lowest collision energy, an isotropic image of the solvated S_N2 product $I^-(H_2O)$ is observed; see Figure 6a. I^- and $I^-(H_2O)$ velocity distributions are mostly indistinguishable as is illustrated by the difference histogram in Figure 5a. The stronger forward tendency of the hydrated product gives a slightly larger estimate of the direct stripping fraction, as shown in Table 1.

The internal energy of the reaction products is quantified by the average total internal excitation, $\langle E_{int} \rangle$, divided by the total available energy, $E_{rel} + E_{exo}$. For the two-body product channel of $I^-(H_2O) + CH_3F$, this quantity can be experimentally determined and is given by $\langle \Delta E \rangle / (E_{rel} + E_{exo})$. One obtains a fraction of 0.76(4) at $E_{rel} = 0.32$ eV. Average fractions and absolute internal energies at all collision energies are given in the Supporting Information. For the three-body product channel involving I^-, which is expected to be the dominant channel,[17] one can also compute the fraction $\langle \Delta E \rangle / (E_{rel} + E_{exo}) = 0.74(6)$. Here, it provides an upper bound to the true internal excitation fraction, due to the relative translational energy between the two neutral products $E_{rel}^{neutral}$ (see eq 1).

Solvation of the I^- product brings an energy gain of 0.45 eV.[49] Inspecting the product relative kinetic energy E_{rel}' (extracted from the measured product velocity vectors) for unsolvated and solvated product ions, we obtain a shift of the
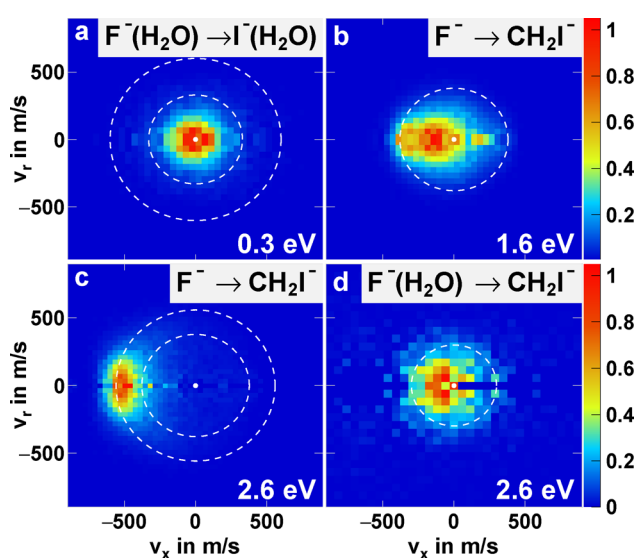

Figure 6. Product ion velocity images in center-of-mass frame of (a) $I^-(H_2O)$ from nucleophilic substitution and (b–d) CH_2I^- from proton transfer in the $F^-(H_2O) + CH_3I$ and $F^- + CH_3I$ reactions at different collision energies. Reactants and collision energies are specified in the images.

mean value from 0.29 to 0.36 eV. Thus, most of the $I^-(H_2O)$ solvation energy, at least 85%, is not partitioned into translational motion, but is retained in product internal excitation.

3.3. Proton Transfer Reactions. The proton transfer product anion CH_2I^- from reactions of hydrated $F^-(H_2O)$ is not observed up to 1.6 eV and appears weakly at 2 eV collision energy. The image at 2.6 eV shows a single broad distribution with a tendency to forward scattering in Figure 6d. It is attributed to the proton transfer to $F^-(H_2O)$ as is detailed in Supporting Information. The observed CH_2I^- branching is 3%, and no solvated $CH_2I^-(H_2O)$ could be detected. The $F^- + CH_3I$ proton transfer reaction at 2.6 eV collision energy in Figure 6c features strong forward scattering near the maximum kinetic energy (see also ref 30). It is less pronounced at 1.6 eV collision energy in Figure 6b, which actually resembles the 2.6 eV image from $F^-(H_2O)$ in terms of angle and energy distribution.

3.4. Reactions of $Cl^-(H_2O)$. A product mass spectrum and I^- velocity images for $Cl^-(H_2O) + CH_3I$ scattering at 0.3 eV
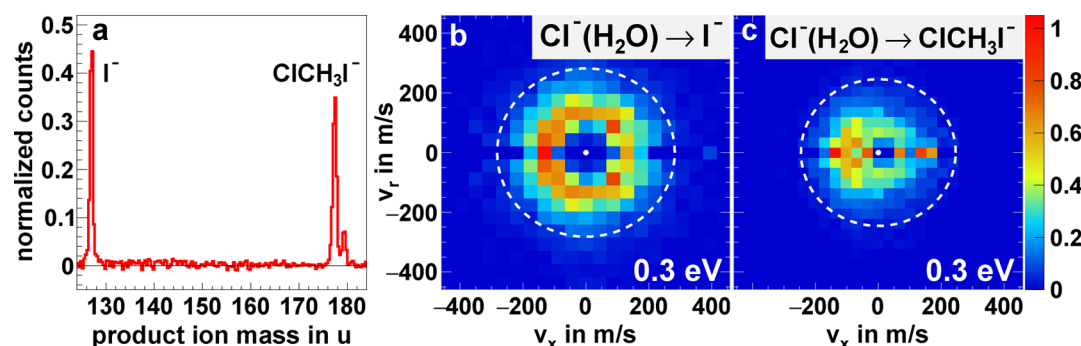
Figure 7. (a) Product mass spectrum and (b) I$^-$ and (c) ClCH$_3$I$^-$ velocity images for the Cl$^-$(H$_2$O) + CH$_3$I reaction at E_{rel} = 0.31(4) eV.

collision energy are shown in Figure 7. The only products are I$^-$ from nucleophilic substitution and ClCH$_3$I$^-$ from ligand exchange in a 54:46 ratio. I$^-$ formation gives rise to a single isotropic distribution without forward or backward flux as is seen for F$^-$(H$_2$O) in Figure 5a, which points toward indirect mechanisms. Interestingly, a ring-shaped structure in Figure 7b reveals a lower bound to the product kinetic energy of about 30 meV. A similar signature is observed in the backward hemisphere of the ClCH$_3$I$^-$ image in Figure 7c, which contains a second broader distribution in the forward direction.

Additional measurements of the Cl$^-$(H$_2$O) + CH$_3$I reaction at 0.6 and 1.1 eV collision energies in the presence of O$_2$$^-$(H$_2$O) show single isotropic I$^-$ distributions with increasing tendency to forward scattering. The presence of ClCH$_3$I$^-$ at these higher collision energies proves that Cl$^-$(H$_2$O) contributes significantly to the observed reactions. However, we do not observe signatures of direct backward scattering. It can therefore be ruled out as a dominant mechanism in the Cl$^-$(H$_2$O) + CH$_3$I reaction at the investigated energies.

4. DISCUSSION

4.1. Product Solvation. Addition of a water molecule to the F$^-$ + CH$_3$I reaction opens new reaction channels including solvation of the neutral or the ionic product, methanol formation following charge transfer in F$^-$(H$_2$O), and ligand exchange. The experiment resolves different product ions with 89(1)% I$^-$, 4.5(9)% I$^-$(H$_2$O), and 6.2(7)% F$^-$(CH$_3$I) at 0.32 eV collision energy. Despite being energetically favored (see Figure 1), I$^-$(H$_2$O) comes up for only 4.8(9)% of S$_N$2 reactivity in excellent agreement with 4.4(13)% from direct dynamics simulations.[17] For comparison, in the isoelectronic reaction of OH$^-$(H$_2$O) with CH$_3$I, only 2.5% of the S$_N$2 products are solvated.[38] This may be attributed to the larger fraction of direct dynamics, which may not leave enough time for the water molecule to interact with the leaving group. In contrast, Cl$^-$(H$_2$O) + CH$_3$I exclusively forms the unsolvated I$^-$ product and Cl$^-$(CH$_3$I) by ligand exchange in a 54:46 ratio. The large fraction of Cl$^-$(CH$_3$I) is indicative of a strong suppression of the S$_N$2 pathway at the lowest collision energy. As solvent transfer in the gas phase S$_N$2 reactions is inefficient and even more suppressed by early water loss at higher collision energies, the absence of solvated products in the Cl$^-$(H$_2$O) + CH$_3$I reaction might be explained by the significantly lower solvation energy (0.64 eV), favoring early water loss, as opposed to F$^-$ (1.01 eV) and OH$^-$ (1.2 eV).[49]

A strong influence of the nucleophile has also been observed in the X$^-$(H$_2$O) + CH$_3$Br reaction at thermal energies in the

200−500 K range. With X$^-$ = OH$^-$, the product Br$^-$(H$_2$O) accounts for about 10% of the S$_N$2 products at the studied temperatures,[50] and for 7−4% in a beam experiment probing collision energies from 0.3 to 1 eV.[11] With F$^-$, up to 20% solvated product ions are observed at 200 K, but they are completely suppressed at 500 K.[13] With Cl$^-$, the S$_N$2 pathway is completely negligible and there is experimental evidence that Cl$^-$(CH$_3$Br) is formed in the Cl$^-$(D$_2$O) + CH$_3$Br reaction.[12]

At higher collision energies, the F$^-$(H$_2$O) + CH$_3$I → I$^-$(H$_2$O) + CH$_3$F pathway is increasingly inhibited. This is in good agreement with the presented trajectory simulations and stems from the fact that higher collision energy leads to water loss at the initial collisional encounter before nucleophilic displacement takes place.[23] The slightly larger solvated fraction found in our trajectory simulations compared to the experiment may be caused by different upper bounds on the lifetime of metastable reaction complexes, which amounts to submicrosecond and picosecond time scales for experiment and trajectory simulations, respectively. Increasing the collision energy in the unsolvated reaction opens proton transfer and dihalide formation as competing pathways to S$_N$2, e.g., in the F$^-$ + CH$_3$I[30] and Cl$^-$ + CH$_3$Br[51] reactions. The observed product mass spectra of the F$^-$(H$_2$O) + CH$_3$I reaction are compatible with dihalide formation, but a clear assignment is precluded by the coreactants. Proton transfer could be attributed to the title reaction (see the Supporting Information) and is further discussed below.

4.2. Long-Lived Intermediates. The solvent-free reactions with F$^-$, OH$^-$, and Cl$^-$ involve different minima of the F$^-$(CH$_3$I), OH$^-$(CH$_3$I), or Cl$^-$(CH$_3$I) complexes[27,32,52] as reaction intermediates on a picosecond time scale.[53] A solvent molecule may leave the intermediate complex with a sufficient amount of kinetic energy to stabilize it and form very long-lived or stable ligand exchange products. Experimental evidence for the latter is absent in the product mass spectra of the monohydrated reactions with Cl$^-$ (Figure 7) and OH$^-$ (ref 39). However, for reactions with F$^-$(H$_2$O) it becomes significant in the measured 11(3)% fraction of I$^-$ products that are observed at apparently higher masses due to dissociation of a complex during acceleration. The fraction is noticeably suppressed by a 2 μs imaging delay. The observed range up to 144 u corresponds to maximum lifetimes of 3−4 μs.

The metastable complex leading to delayed I$^-$ product formation may either be the solvated product anion or the ligand exchange complex. The I$^-$ fraction from metastable complexes is larger than the I$^-$(H$_2$O) branching. In direct dynamics simulations only 12% of the I$^-$(H$_2$O) products have internal energies above the dissociation threshold at the end of trajectories.[17] This implies the alternative option of FCH$_3$I$^-$

complex formation by ligand exchange with subsequent S_N2 reaction and dissociation in line with the new QCT trajectories with FCH_3I^- complexes that are in parts still reactive at $20a_0$ separation from the neutral. The reaction may be trapped in the halogen-bonded $FICH_3^-$, hydrogen-bonded $F^-\cdots HCH_2I$, or ion–dipole $F^-\cdots CH_3I$ prereaction complexes.[27] The latter undergoes Walden inversion with a transition state 1.29 eV above the $I^- + CH_3F$ asymptote. Trapping in the postreaction complex $I^-\cdots CH_3F$ thus requires an unlikely late water loss to absorb most of this energy after the nucleophilic displacement. We speculate that metastable complexes are either susceptible to stimulated dissociation by moderate forces during acceleration (see Figure S3.3), or the likelihood of dissociation before 5 μs is too small to detect I^- products in the 144−161 u range. Transient trapping in the water-free reaction intermediate in 70% of the indirect $F^-(H_2O) + CH_3I$ reactions at 1.53 eV[23] further supports that metastable complexes formed by ligand exchange are responsible for the delayed I^- production.

Trapping in the halogen-bonded front-side complex plays a role in the solvent-free $F^- + CH_3I$ reaction[26] and is a candidate for a ligand exchange intermediate. However, a high barrier impedes dissociation to I^- via the front-side attack mechanism. In the OH^- system, energetics moreover preclude trapping in a prereaction complex and, at higher collision energies, $HO^-\cdots HCH_2I$ is expected to pass the S_N2 transition state quickly and dissociate.[16] This should be similar in the case of the ion–dipole complexes with Cl^- and F^-. For the reaction with $F^-(CH_3I)$, we single out the hydrogen-bonded $F^-\cdots HCH_2I$ as the most likely long-lived intermediate that gives rise to the observed dissociation at microsecond time scales—in line with about 90% of the indirect mechanisms passing through this complex in direct dynamics simulations.[17] Also the front-side complex may be important, if I^- shifts toward a hydrogen atom and S_N2 occurs via the hydrogen-bonded complex.

4.3. Mechanisms. Improved resolution of the I^- images from $F^- + CH_3I$ scattering permits us to quantify direct rebound (DR), direct stripping (DS), and indirect mechanisms in a 12:19:69 ratio at 0.3 eV. Selecting a minimum internal excitation of 1.2 eV in this analysis gives a smaller fraction of 52% indirect reactions, in better agreement with chemical dynamics calculations. Direct dynamics simulations using DFT/B97-1 electronic structure theory obtained 15(2), 25(3) and 60(4)%[28] for DR, DS, and indirect mechanisms, while QCT simulations on a PES at the CCSD(T) level yield 17:23:60.[29] B97-1 results at 1.53 eV collision energy also found a large fraction of 59% indirect mechanism. However, this has been refuted by more recent calculations, which yield 46:43:11 using direct dynamics at the MP2 level[54] and 49:31:20 from the CCSD(T) level simulations at 1.53 eV collision energy.[29] Our experimental results at 1.56 eV give 41% DR, 43% sideways stripping, 6% forward, and 10% low energy isotropic scattering. This indirect fraction compares well with the two recent computational results, in particular when considering that the CCSD(T) value includes indirect events with high product ion velocities that have not been captured by the experimental analysis. Overall, this now confirms the transition from dominantly indirect reactions at low collision energies to two different direct mechanisms at higher collision energy, in contrast to earlier findings.[28]

In the angular distributions, the minima for the I^- and $I^-(H_2O)$ products in the $F^-(H_2O) + CH_3I$ reaction shift to the forward direction. This is in contrast to the sideways minima in

the bare F^- case. In recent simulations, DR extends to forward scattering angles near $\cos(\theta) = 0.3$ (see Figure S2 in the Supporting Information of ref 23). This supports our procedure to separate forward and backward scattering at the minimum of the angular distributions. At the same time, it shows that DR and DS sum up to a non-negligible part of the isotropic area in the angular distribution such that the indirect fractions in Table 1 are upper bound estimates.

The derived 13(2)% DR of I^- products at 0.3 eV (see Table 1) match well with the 14% from direct dynamics simulations.[17] The 4(2)% DS contribution is smaller than the direct dynamics value of 16%, which hints at an underestimation of DS due to imperfect separation in the angular distributions. In the $I^-(H_2O)$ channel, the simulations predict 32% DR and the absence of DS. This should lead to stronger backward scattering as for the I^- products, which is contradicted by the almost identical angular distributions of the two products. Below 1.6 eV the DR and DS fractions stay roughly constant. The transition from dominantly indirect to direct mechanisms that is found for the unsolvated reaction is therefore strongly suppressed by the solvent molecule. Toward 2.6 eV the derived DR contribution grows, but only from 13 to 19%, while the DS fraction remains small. This is explained by early water loss in high energy collisions.[23] However, this does not affect the DS fraction, which may have to do with different impact parameter ranges for the two mechanisms. Theoretical calculations seem to overestimate the decrease of the indirect fraction with 71 and 57% as opposed to constant 83% observed near both 0.3 and 1.6 eV collision energies.[23] This discrepancy may be caused by the ambiguity that occurs when the fraction of indirect reactions is estimated from product ion angular distributions in the three-body dissociation into I^-, CH_3F, and H_2O. Future experiments using coincident detection of two products may overcome this.

The angular distributions from the presented trajectory simulations agree with the close similarity for I^- and $I^-(H_2O)$ at the lowest collision energy, but there are also differences. Due to larger forward and backward scattering intensities, the simulation results are less isotropic. The observed asymmetry with a minimum intensity at forward directions only appears at higher energies. Finally, the observed 2.6 eV tendency to stronger backward scattering is much stronger and is already seen at 1 eV.

There is no sign of the appearance of DR in the $Cl^-(H_2O) + CH_3I$ reaction between 0.3 and 1.1 eV collision energies. Direct dynamics simulations at 1.9 eV predict dominant DR and an important indirect roundabout mechanism.[24] Crossed beam imaging of the solvent-free $Cl^- + CH_3I$ reaction showed a transition to dominant DR already near 0.5 eV collision energy.[31,36] DR is nearly the only pathway at 1.1 eV and is complemented by the roundabout mechanism at 1.9 eV.[31] Our measurements therefore confirm the expectation of efficiently suppressed direct mechanisms up to relatively high collision energies. Theory predicts internal energy and angular distributions similar to the unsolvated system due to early water loss in higher energy collisions, which demands further experiments for verification. At 0.3 eV collision energy, a ring-shaped I^- product velocity image is reminiscent of the $ClCH_3I^-$ image of the ligand exchange pathway. In the latter case, an additional broader distribution in the forward direction is observed and attributed to high impact parameters. We speculate that lower impact parameters could allow transfer of the collision energy into internal excitation and

nucleophilic substitution could occur only indirectly via the ligand exchange intermediate.

4.4. Energy Partitioning. Besides the strong similarity of I^- and $I^-(H_2O)$ angular distributions in the $F^-(H_2O)$ reaction at 0.32 eV, also the average fraction of product energy partitioned into internal excitation is found to be very similar for both ions, provided the relative energy between the neutral products CH_3F and H_2O is included in the case of I^- formation (see Results). The fraction of product excitation differs by the fraction that is channeled into relative kinetic energy between the neutral products in the case of I^- formation. At least 85% of the solvation energy (0.45 eV) gained by $I^-(H_2O)$ formation is retained in product internal excitation. This suggests that CH_3F departs quickly once H_2O attaches to I^- such that little of the solvation energy is channeled into kinetic energy. As $I^-(H_2O)$ excitation must be smaller than the dissociation energy, we can attribute a minimum fraction of 0.44 to CH_3F internal excitation in comparison to 0.67(2) in the unsolvated reaction. The latter is 10% smaller than the total internal energy fraction 0.74(6) in the solvated case, in agreement with a stronger contribution of direct mechanisms.

At 1.56 eV, the internal energy fraction of the solvent-free reaction drops to 0.58(2), which is not fully reproduced by theory with fractions of 0.69(2) and 0.66(1).[23] In the solvated reaction it stays almost constant with 0.74(6) and then drops to 0.69(3) at 2.6 eV due to the increased DR fraction. These fractions correspond to internal energies, including relative motion of the neutrals, of 0.70(2) and 1.62(2) eV at 0.32 and 1.55 eV collision energy, respectively. These values are comparable with the respective quantities of 0.77(1) and 1.71(4) eV, obtained from direct dynamics simulation.[23,55]

4.5. Proton Transfer. Without a barrier[22] and with 1.89 eV endothermicity, proton transfer is expected to open up at collision energies about 1.1 eV higher than in the $F^- + CH_3I$ reaction with an endothermicity of 0.71 eV (see Figure 1). This is confirmed by the observed appearance of a small fraction at 2 eV collision energy and above. The CH_2I^- product image at 2.6 eV, 0.7 eV above the predicted threshold, gives a similar dynamical fingerprint in terms of angle and energy distributions as the unsolvated proton transfer at 1.6 eV, about 0.9 eV above threshold, which corresponds to a similar excess energy as is indicated in Figure 1. This agrees well with very similar stationary point geometries of the unsolvated and solvated systems[22] along the proton transfer pathway. Due to the high collision energy, the fluorine anion and water molecule dissociate easily at the initial collision and then propagate separately on opposite sides of the methyl group. In this way, the additional collision energy is consumed by dissociation, and otherwise, the reaction occurs similar to the unsolvated one. The energetically favored solvated product ion has not been detected. Considering the noise level, it is suppressed by roughly a factor of not less than 5 relative to CH_2I^- formation.

5. CONCLUSIONS

Product branching ratios as well as angle and energy-differential cross sections have been obtained using crossed beam imaging and quasiclassical trajectory calculations. The $F^-(H_2O) + CH_3I$ reaction in comparison to $F^- + CH_3I$ and the $Cl^-(H_2O) + CH_3I$ reaction were investigated at different collision energies starting at 0.3 eV. At the lowest collision energy, the $F^-(H_2O) + CH_3I$ reaction forms the S_N2 products

I^- and $I^-(H_2O)$ as well as the ligand switching product FCH_3I^- in a 89:5:6 branching. The suppression of the energetically favored product $I^-(H_2O)$, which we have also seen for $OH^-(H_2O)$, grows at higher collision energies, in very good agreement between experiment and simulation.

Indirect reaction dynamics, evidenced by isotropic scattering with large product internal excitations, dominate the reaction dynamics for $F^-(H_2O)$ as well as for $Cl^-(H_2O)$. This differs from the reactions of the unsolvated nucleophiles, where direct reaction mechanisms are more important. The quasiclassical trajectory simulations show overall good agreement with the measured angular distributions. They show a larger probability for forward and backward scattering than observed in the experiment, which still needs an explanation.

Further analysis of the QCT results will allow us to investigate the relative energy partitioning into the different translational and internal degrees of freedom of the reaction products. This will be particularly interesting for the nonsolvated product channels, which dominate the reactivity and lead to three different reaction products. The experiment can only detect the charged product, but together with the simulations the three-particle correlations and the amount of translational and internal energy partitioned into the two neutral molecules become accessible.

The present experiments have been hampered by coreactants that have complicated the analysis significantly. Future experiments are planned with an improved suppression of small fractions of nearby reactant masses. This will allow us to also study reactions with two or even more solvent molecules attached to the nucleophile. Furthermore, it will be interesting to compare the reaction dynamics for very different solvent molecules, such as carbon dioxide or acetonitrile.

■ ASSOCIATED CONTENT

Ⓢ Supporting Information

The Supporting Information is available free of charge at https://pubs.acs.org/doi/10.1021/acs.jpca.0c00098.

Computed exothermicities for all reactants and coreactants (PDF)

Analysis of product branchings and coreactant contributions (PDF)

Average internal energies, apparent masses, and acceleration (PDF)

■ AUTHOR INFORMATION

Corresponding Author

  Roland Wester − *Institut für Ionenphysik und Angewandte Physik, Universität Innsbruck, 6020 Innsbruck, Austria;* ⊙ orcid.org/0000-0001-7935-6066; Phone: +43 (0)512 507 52620; Email: roland.wester@uibk.ac.at

Authors

  Björn Bastian − *Institut für Ionenphysik und Angewandte Physik, Universität Innsbruck, 6020 Innsbruck, Austria*

  Tim Michaelsen − *Institut für Ionenphysik und Angewandte Physik, Universität Innsbruck, 6020 Innsbruck, Austria*

  Lulu Li − *State Key Laboratory of Molecular Reaction Dynamics, Dalian Institute of Chemical Physics, Chinese Academy of Sciences, Dalian, Liaoning 116023, China*

  Milan Ončák − *Institut für Ionenphysik und Angewandte Physik, Universität Innsbruck, 6020 Innsbruck, Austria;* ⊙ orcid.org/0000-0002-4801-3068

Jennifer Meyer − *Institut für Ionenphysik und Angewandte Physik, Universität Innsbruck, 6020 Innsbruck, Austria*

Dong H. Zhang − *State Key Laboratory of Molecular Reaction Dynamics, Dalian Institute of Chemical Physics, Chinese Academy of Sciences, Dalian, Liaoning 116023, China*

Complete contact information is available at:
https://pubs.acs.org/10.1021/acs.jpca.0c00098

Notes

The authors declare no competing financial interest.

REFERENCES

(1) Carrascosa, E.; Meyer, J.; Wester, R. Imaging the Dynamics of Ion−Molecule Reactions. *Chem. Soc. Rev.* **2017**, *46*, 7498−7516.

(2) Meyer, J.; Wester, R. Ion−Molecule Reaction Dynamics. *Annu. Rev. Phys. Chem.* **2017**, *68*, 333−353.

(3) Xie, J.; Otto, R.; Mikosch, J.; Zhang, J.; Wester, R.; Hase, W. L. Identification of Atomic-Level Mechanisms for Gas-Phase X^- + CH_3Y S_N2 Reactions by Combined Experiments and Simulations. *Acc. Chem. Res.* **2014**, *47*, 2960−2969.

(4) Szabó, I.; Czakó, G. Dynamics and Novel Mechanisms of S_N2 Reactions on ab Initio Analytical Potential Energy Surfaces. *J. Phys. Chem. A* **2017**, *121*, 9005−9019.

(5) Tasi, D. A.; Fábián, Z.; Czakó, G. Rethinking the X^- + CH_3Y [X = OH, SH, CN, NH_2, PH_2; Y = F, Cl, Br, I] S_N2 Reactions. *Phys. Chem. Chem. Phys.* **2019**, *21*, 7924−7931.

(6) Orr-Ewing; Perspective, A. J. Bimolecular Chemical Reaction Dynamics in Liquids. *J. Chem. Phys.* **2014**, *140*, 090901.

(7) Craig, S. L.; Brauman, J. I. Intramolecular Microsolvation of S_N2 Transition States. *J. Am. Chem. Soc.* **1999**, *121*, 6690−6699.

(8) Chandrasekhar, J.; Smith, S. F.; Jorgensen, W. L. S_N2 Reaction Profiles in the Gas Phase and Aqueous Solution. *J. Am. Chem. Soc.* **1984**, *106*, 3049−3050.

(9) Hierl, P. M.; Ahrens, A. F.; Henchman, M. J.; Viggiano, A. A.; Paulson, J. F.; Clary, D. C. Chemistry as a Function of Solvation Number. Solvated-Ion Reactions in the Gas Phase and Comparison with Solution. *Faraday Discuss. Chem. Soc.* **1988**, *85*, 37−51.

(10) Bohme, D. K.; Raksit, A. B. Gas-Phase Measurements of the Influence of Stepwise Solvation on the Kinetics of S_N2 Reactions of Solvated F^- with CH_3Cl and CH_3Br and of Solvated Cl^- with CH_3Br. *Can. J. Chem.* **1985**, *63*, 3007−3011.

(11) Henchman, M.; Paulson, J. F.; Hierl, P. M. Nucleophilic Displacement with a Selectively Solvated Nucleophile: The System $OH^- \cdot H_2O$ + CH_3Br at 300 K. *J. Am. Chem. Soc.* **1983**, *105*, 5509−5510.

(12) Seeley, J. V.; Morris, R. A.; Viggiano, A. A.; Wang, H. B.; Hase, W. L. Temperature Dependence of the Rate Constants and Branching Ratios for the Reactions of $Cl^-(D_2O)_{1-3}$ with CH_3Br and Thermal Dissociation Rates for $Cl^-(CH_3Br)$. *J. Am. Chem. Soc.* **1997**, *119*, 577−584.

(13) Seeley, J. V.; Morris, R. A.; Viggiano, A. A. Temperature Dependences of the Rate Constants and Branching Ratios for the Reactions of $F^-(H_2O)_{0-5}$ with CH_3Br. *J. Phys. Chem. A* **1997**, *101*, 4598−4601.

(14) O'Hair, R. A. J.; Davico, G. E.; Hacaloglu, J.; Dang, T. T.; DePuy, C. H.; Bierbaum, V. M. Measurements of Solvent and Secondary Kinetic Isotope Effects for the Gas-Phase S_N2 Reactions of Fluoride with Methyl Halides. *J. Am. Chem. Soc.* **1994**, *116*, 3609−3610.

(15) Zhang, J.; Yang, L.; Sheng, L. Electronic Structure Theory Study of the Microsolvated $F^-(H_2O)$ + CH_3I S_N2 Reaction. *J. Phys. Chem. A* **2016**, *120*, 3613−3622.

(16) Xie, J.; Otto, R.; Wester, R.; Hase, W. L. Chemical Dynamics Simulations of the Monohydrated $OH^-(H_2O)$ + CH_3I Reaction. Atomic-Level Mechanisms and Comparison with Experiment. *J. Chem. Phys.* **2015**, *142*, 244308.

(17) Zhang, J.; Yang, L.; Xie, J.; Hase, W. L. Microsolvated $F^-(H_2O)$ + CH_3I S_N2 Reaction Dynamics. Insight into the Suppressed Formation of Solvated Products. *J. Phys. Chem. Lett.* **2016**, *7*, 660−665.

(18) Liu, X.; Xie, J.; Zhang, J.; Yang, L.; Hase, W. L. Steric Effects of Solvent Molecules on S_N2 Substitution Dynamics. *J. Phys. Chem. Lett.* **2017**, *8*, 1885−1892.

(19) Tachikawa, H. Collision Energy Dependence on the Micro-solvated S_N2 Reaction of $F^-(H_2O)$ with CH_3Cl: A Full Dimensional Ab Initio Direct Dynamics Study. *J. Phys. Chem. A* **2001**, *105*, 1260−1266.

(20) Tachikawa, H. Direct Ab Initio Molecular Dynamics Study on a Microsolvated S_N2 Reaction of $OH^-(H_2O)$ with CH_3Cl. *J. Chem. Phys.* **2006**, *125*, 133119.

(21) Olasz, B.; Czakó, G. High-Level-Optimized Stationary Points for the $F^-(H_2O)$ + CH_3I System: Proposing a New Water-Induced Double-Inversion Pathway. *J. Phys. Chem. A* **2019**, *123*, 454−462.

(22) Liu, X.; Yang, L.; Zhang, J.; Sun, J. Competition of F/OH-Induced S_N2 and Proton-Transfer Reactions with Increased Solvation. *J. Phys. Chem. A* **2018**, *122*, 9446−9453.

(23) Yang, L.; Liu, X.; Zhang, J.; Xie, J. Effects of Microsolvation on a S_N2 Reaction: Indirect Atomistic Dynamics and Weakened Suppression of Reactivity. *Phys. Chem. Chem. Phys.* **2017**, *19*, 9992−9999.

(24) Gu, M.; Liu, X.; Yang, L.; Sun, S.; Zhang, J. Dynamics of $Cl^-(H_2O)$ + CH_3I Substitution Reaction: The Influences of Solvent and Nucleophile. *J. Phys. Chem. A* **2019**, *123*, 2203−2210.

(25) Zhang, J.; Mikosch, J.; Trippel, S.; Otto, R.; Weidemüller, M.; Wester, R.; Hase, W. L. F^-+CH_3I→FCH_3+I^- Reaction Dynamics. Nontraditional Atomistic Mechanisms and Formation of a Hydrogen-Bonded Complex. *J. Phys. Chem. Lett.* **2010**, *1*, 2747−2752.

(26) Szabó, I.; Olasz, B.; Czakó, G. Deciphering Front-Side Complex Formation in S_N2 Reactions via Dynamics Mapping. *J. Phys. Chem. Lett.* **2017**, *8*, 2917−2923.

(27) Olasz, B.; Czakó, G. Uncovering the Role of the Stationary Points in the Dynamics of the F^- + CH_3I Reaction. *Phys. Chem. Chem. Phys.* **2019**, *21*, 1578−1586.

(28) Mikosch, J.; Zhang, J.; Trippel, S.; Eichhorn, C.; Otto, R.; Sun, R.; DeJong, W.; Weidemüller, M.; Hase, W. L.; Wester, R. Indirect Dynamics in a Highly Exoergic Substitution Reaction. *J. Am. Chem. Soc.* **2013**, *135*, 4250−4259.

(29) Olasz, B.; Szabó, I.; Czakó, G. High-level Ab Initio Potential Energy Surface and Dynamics of the F^- + CH_3I S_N2 and Proton-Transfer Reactions. *Chem. Sci.* **2017**, *8*, 3164−3170.

(30) Carrascosa, E.; Michaelsen, T.; Stei, M.; Bastian, B.; Meyer, J.; Mikosch, J.; Wester, R. Imaging Proton Transfer and Dihalide Formation Pathways in Reactions of F^- + CH_3I. *J. Phys. Chem. A* **2016**, *120*, 4711−4719.

(31) Mikosch, J.; Trippel, S.; Eichhorn, C.; Otto, R.; Lourderaj, U.; Zhang, J. X.; Hase, W. L.; Weidemüller, M.; Wester, R. Imaging Nucleophilic Substitution Dynamics. *Science* **2008**, *319*, 183−186.

(32) Zhang, J.; Lourderaj, U.; Sun, R.; Mikosch, J.; Wester, R.; Hase, W. L. Simulation Studies of the Cl^- + CH_3I S_N2 Nucleophilic Substitution Reaction: Comparison with Ion Imaging Experiments. *J. Chem. Phys.* **2013**, *138*, 114309.

(33) Yu, F. Dynamic Exit-Channel Pathways of the Microsolvated $HOO^-(H_2O)$ + CH_3Cl S_N2 Reaction: Reaction Mechanisms at the

Atomic Level from Direct Chemical Dynamics Simulations. *J. Chem. Phys.* **2018**, *148*, 014302.

(34) Liu, X.; Zhang, J.; Yang, L.; Hase, W. L. How a Solvent Molecule Affects Competing Elimination and Substitution Dynamics. Insight into Mechanism Evolution with Increased Solvation. *J. Am. Chem. Soc.* **2018**, *140*, 10995−11005.

(35) Carrascosa, E.; Meyer, J.; Zhang, J.; Stei, M.; Michaelsen, T.; Hase, W. L.; Yang, L.; Wester, R. Imaging the Fingerprints of Competing E2 and S_N2 Reactions. *Nat. Commun.* **2017**, *8*, 25.

(36) Carrascosa, E.; Meyer, J.; Michaelsen, T.; Stei, M.; Wester, R. Conservation of Direct Dynamics in Sterically Hindered S_N2/E2 Reactions. *Chem. Sci.* **2018**, *9*, 693−701.

(37) Otto, R.; Brox, J.; Stei, M.; Trippel, S.; Best, T.; Wester, R. Single Solvent Molecules Can Affect the Dynamics of Substitution Reactions. *Nat. Chem.* **2012**, *4*, 534−538.

(38) Otto, R.; Brox, J.; Trippel, S.; Stei, M.; Best, T.; Wester, R. Exit Channel Dynamics in a Micro-Hydrated S_N2 Reaction of the Hydroxyl Anion. *J. Phys. Chem. A* **2013**, *117*, 8139−8144.

(39) Otto, R.; Xie, J.; Brox, J.; Trippel, S.; Stei, M.; Best, T.; Siebert, M. R.; Hase, W. L.; Wester, R. Reaction Dynamics of Temperature-Variable Anion Water Clusters Studied with Crossed Beams and by Direct Dynamics. *Faraday Discuss.* **2012**, *157*, 41−57.

(40) Eppink, A. T. J. B.; Parker, D. H. Velocity Map Imaging of Ions and Electrons using Electrostatic Lenses: Application in Photoelectron and Photofragment Ion Imaging of Molecular Oxygen. *Rev. Sci. Instrum.* **1997**, *68*, 3477−3484.

(41) Wester, R. Velocity Map Imaging of Ion−Molecule Reactions. *Phys. Chem. Chem. Phys.* **2014**, *16*, 396−405.

(42) *SIMION Ion Optics Simulation Software*, version 8.1; Scientific Instrument Services, Inc.: 2013.

(43) Stei, M.; von Vangerow, J.; Otto, R.; Kelkar, A. H.; Carrascosa, E.; Best, T.; Wester, R. High Resolution Spatial Map Imaging of a Gaseous Target. *J. Chem. Phys.* **2013**, *138*, 214201.

(44) Mikosch, J.; Frühling, U.; Trippel, S.; Otto, R.; Hlavenka, P.; Schwalm, D.; Weidemüller, M.; Wester, R. Evaporation of Trapped Anions Studied with a 22-Pole Ion Trap in Tandem Time-of-Flight Configuration. *Phys. Rev. A: At., Mol., Opt. Phys.* **2008**, *78*, 023402.

(45) Frisch, M. J.; Trucks, G. W.; Schlegel, H. B.; Scuseria, G. E.; Robb, M. A.; Cheeseman, J. R.; Scalmani, G.; Barone, V.; Petersson, G. A.; Nakatsuji, H.; et al. *Gaussian 16*, revision A.3; Gaussian, Inc.: Wallingford, CT, 2016.

(46) Shao, K.; Chen, J.; Zhao, Z.; Zhang, D. H. Communication: Fitting Potential Energy Surfaces with Fundamental Invariant Neural Network. *J. Chem. Phys.* **2016**, *145*, 071101.

(47) Zhang, I. Y.; Xu, X.; Jung, Y.; Goddard, W. A. A Fast Doubly Hybrid Density Functional Method Close to Chemical Accuracy Using a Local Opposite Spin Ansatz. *Proc. Natl. Acad. Sci. U. S. A.* **2011**, *108*, 19896−19900.

(48) Frisch, M. J.; Trucks, G. W.; Schlegel, H. B.; Scuseria, G. E.; Robb, M. A.; Cheeseman, J. R.; Scalmani, G.; Barone, V.; Mennucci, B.; Petersson, G. A.; et al. *Gaussian 09*, revision C.1; Gaussian, Inc.: Wallingford, CT, 2010.

(49) Hiraoka, K.; Mizuse, S.; Yamabe, S. Solvation of Halide Ions with Water and Acetonitrile in the Gas Phase. *J. Phys. Chem.* **1988**, *92*, 3943−3952.

(50) Viggiano, A. A.; Arnold, S. T.; Morris, R. A.; Ahrens, A. F.; Hierl, P. M. Temperature Dependences of the Rate Constants and Branching Ratios for the Reactions of $OH^-(H_2O)_{0-4}$ + CH_3Br. *J. Phys. Chem.* **1996**, *100*, 14397−14402.

(51) Cyr, D. M.; Scarton, M. G.; Wiberg, K. B.; Johnson, M. A.; Nonose, S.; Hirokawa, J.; Tanaka, H.; Kondow, T.; Morris, R. A.; Viggiano, A. A. Observation of the XY^- Abstraction Products in the Ion−Molecule Reactions X^- + RY → XY^- + R: An Alternative to the S_N2 Mechanism at Suprathermal Collision Energies. *J. Am. Chem. Soc.* **1995**, *117*, 1828−1832.

(52) Xie, J.; McClellan, M.; Sun, R.; Kohale, S. C.; Govind, N.; Hase, W. L. Direct Dynamics Simulation of Dissociation of the $[CH_3−I−OH]^-$ Ion−Molecule Complex. *J. Phys. Chem. A* **2015**, *119*, 817−825.

(53) Mikosch, J.; Otto, R.; Trippel, S.; Eichhorn, C.; Weidemüller, M.; Wester, R. Inverse Temperature Dependent Lifetimes of Transient S_N2 Ion-Dipole Complexes. *J. Phys. Chem. A* **2008**, *112*, 10448−10452.

(54) Sun, R.; Davda, C. J.; Zhang, J.; Hase, W. L. Comparison of Direct Dynamics Simulations with Different Electronic Structure Methods. F^- + CH_3I with MP2 and DFT/B97−1. *Phys. Chem. Chem. Phys.* **2015**, *17*, 2589−2597.

(55) Zhang, J.; Yang, L. Additional information for ref 23 from private communication, November 2019.